

Raman Scattered He II λ 6545 in the Young and Compact Planetary Nebula NGC 6790

Eun-Ha Kang¹, Byeong-Cheol Lee² & Hee-Won Lee¹

¹ Department of Astronomy and Space Science, Astrophysical Research Center for the Structure and Evolution of the Cosmos, Sejong University, Seoul, 143-747, Korea

² Department of Astronomy and Atmospheric Sciences, Kyungpook National University

hwlee@sejong.ac.kr

Received _____; accepted _____

Submitted to ApJ

ABSTRACT

We present the high resolution spectra of the young and compact planetary nebula NGC 6790 obtained with the echelle spectrograph at Bohyunsan Optical Astronomy Observatory and report the discovery of Raman scattered He II λ 6545 in this object. This line feature is formed in a thick neutral region surrounding the hot central star, where He II λ 1025 line photons are scattered inelastically by hydrogen atoms. A Monte Carlo technique is adopted to compute the line profiles with a simple geometric model, in which the neutral region is in the form of a cylindrical shell that is expanding from the central star. From our line profile analysis, the expansion velocity of the H I region lies in the range $v_{exp} = 15 - 19 \text{ km s}^{-1}$. Less stringent constraints are put on the H I column density N_{HI} and covering factor C , where the total flux of Raman He II λ 6545 is consistent with their product $CN_{HI} \sim 0.5 \times 10^{20} \text{ cm}^{-2}$. The Monte Carlo profiles from stationary emission models exhibit deficit in the wing parts. A much better fit is obtained when the He II emission region is assumed to take the form of a ring that slowly rotates with a rotation speed $\sim 18 \text{ km s}^{-1}$. Brief discussions are presented regarding the mass loss processes and future observations.

Subject headings: planetary nebulae — planetary nebulae: individual NGC 6790 — radiative transfer — scattering — mass loss

1. Introduction

Mass loss is an important process that mainly occurs in the late stage of stellar evolution. A star with a mass less than $8 M_{\odot}$ loses a significant amount of mass in the giant stage before becoming a planetary nebula with a hot white dwarf at its center. Considering the Chandrasekhar limit of $1.4 M_{\odot}$, the mass loss process in the giant stage with enriched heavy elements should be important in the chemical evolution of the interstellar medium. In this regard, with a recent history of mass loss, young planetary nebulae are interesting objects to study the mass loss process.

It is expected that around a young planetary nebula there may be a significant amount of neutral material that was lost in the previous stage of stellar evolution. In this case, the neutral region is exposed to the strong UV emission line source in the vicinity of the hot central star of the planetary nebula. Therefore, important information related with the mass loss process can be gathered from investigations of the scattering processes of the UV radiation originating from the center region.

Taylor, Gussie & Pottasch (1990) performed H I 21 cm radio observations for a number of compact planetary nebulae (see also Altschuler et al. 1986, Gussie & Taylor 1995, Schneider et al. 1987). Their target selection was made on the basis of high radio brightness temperature, which is indicative of the nebular compactness. They searched an absorption trough that may be formed at the radial velocity of a compact planetary nebula when the neutral region blocks the background H I radio emission from our Galaxy. A number of compact young planetary nebulae including IC 5117 and NGC 6790 have been detected. Adopting an excitation temperature $T_{HI} = 100$ K, the typical H I column density was determined to be of order $N_{HI} \sim 10^{20} \text{ cm}^{-2}$ in these objects.

Astrophysical Raman spectroscopy involving atomic hydrogen was initiated by Schmid (1989), who identified the mysterious broad emission bands occurring at 6825 \AA and 7088

Å in many symbiotic stars (see also Nussbaumer, Schmid & Vogel 1989). He proposed that a hydrogen atom in the ground state is excited with the absorption of an incident far UV O VI λ 1032 photon and de-excites into the $2s$ level with the re-emission of an optical photon at 6825 Å. An analogous process for far UV O VI λ 1038 yields optical photons at 7088 Å. The large line width and prominent linear polarization exhibited by these scattered features strongly support his proposal (e.g. Harries & Howarth 1996). Observations made simultaneous in the UV and optical regions also confirm the Raman scattering nature (Espey et al. 1995).

In the spectrum of the symbiotic star RR Telescopii, Van Groningen (1993) discovered Raman scattered He II features that are formed blueward of hydrogen Balmer emission lines. He II emission lines arising from transitions between $n = 2k$ and $n = 2$ levels have wavelengths that are slightly shorter than hydrogen Lyman lines owing to the fact that He II ions are single electron atoms with a slightly larger two body reduced mass. The proximity to resonance is responsible for a large scattering cross section requiring the existence of a neutral region with $N_{HI} \sim 10^{20}$ cm $^{-2}$ around a He II emission source. Raman scattered He II features are also reported in other symbiotic stars including He 2-106, HM Sagittae and V1016 Cygni (Lee, Kang & Byun 2001, Jung & Lee 2004b, Birriel 2004).

Raman scattering of He II by atomic hydrogen also operates in young planetary nebulae. The first discovery was reported by Péquignot et al. (1997) in their spectroscopic analysis of the young planetary nebula NGC 7027. Subsequently, Groves et al. (2002) found the same Raman scattered He II features in the planetary nebula NGC 6302. Recently, Lee et al. (2006) reported that the compact planetary nebula IC 5117 also exhibits Raman scattered He II features blueward of H α and H β . In these objects, it appears that the central star is surrounded by a neutral region with a significant covering factor. In particular, Lee et al. (2006) discussed in detail the atomic physics of He II recombination

and Raman scattering processes.

We present our high resolution spectra of the young and compact planetary nebula NGC 6790 and report our finding of the Raman scattered He II λ 6545 feature in this object. Using the H α image, Tytenda et al. (2003) measured the angular size of NGC 6790 to be $4'' \times 3''$. This size estimate of NGC 6790 is consistent with the HST image shown by Kwok, Su & Sahai (2003), who also identified two inner shells of similar orientations in NGC 6790. The distance to NGC 6790 is poorly known. Gathier et al. (1986) proposed that NGC 6790 is further than ~ 0.8 kpc based on their kinematic considerations. Adopting a statistical method Zhang (1995) suggested a distance of 5.7 kpc to NGC 6790. In their high resolution spectroscopy of NGC 6790, Aller, Hyung & Feibelman (1996) proposed a core mass of $0.6 M_{\odot}$ and an age of 6000 yr with the note that these values are dependent on the uncertain distance to NGC 6790.

We perform Monte Carlo radiative transfer simulations in order to obtain the geometric and kinematic information of the neutral region. In section 2, we describe our observation and line fitting analyses and the following section presents our results of the Monte Carlo radiative transfer. In the final section, we discuss briefly our observation and mass loss processes of NGC 6790.

2. Observation and Analysis

2.1. Observation and Data

We observed the young planetary nebula NGC 6790 on the night of 2008 May 31 using the 1.8 m telescope at Bohyunsan Optical Astronomy Observatory (BOAO). The spectrograph that we used is the BOES (BOAO Echelle Spectrograph), which is a bench-mounted echelle system fed by optical fibers with various diameters. We used the

300 micron fiber, which yields the spectral resolution $\sim 30,000$ with the field of view of $3''$. The spectral coverage ranges 3600 \AA through $10,500 \text{ \AA}$. We obtained two spectra with exposure times of 600 s and 7200 s, respectively. A Th-Ar lamp was used for wavelength calibrations. For more detailed information on BOES, one is referred to Kim et al. (2007). Standard procedures using the IRAF packages were followed to reduce the spectra.

In Fig. 1, we show parts of our spectra around $H\alpha$ and $H\beta$. The vertical axis represents the relative flux density. We normalize the flux density using $[\text{N II}]\lambda 6548$, which is set to have a flux density peak of unity. The top panel of Fig. 1 is the spectrum around $H\alpha$ with an exposure time of 600 s. We note strong forbidden emission lines of N II at 6548 \AA and 6583 \AA . In this short exposure spectral image, the strongest $H\alpha$ is unsaturated, allowing us to fit the $H\alpha$ profile. The middle panel of Fig. 1 shows the $H\alpha$ part of the spectrum with an exposure time of 7200 s. The strong $H\alpha$ is saturated and we can discern very faint emission lines including $\text{He II}\lambda 6527$. $\text{He II}\lambda 6527$ arises from transitions between $n = 14$ and $n = 5$ levels. We also clearly notice that around $[\text{N II}]\lambda 6548$ there exists a broad bump-like feature. This feature is not an instrumental artifact because no such feature is present near $[\text{N II}]\lambda 6583$, which is supposed to be 3 times stronger than $[\text{N II}]\lambda 6548$ (e.g. Osterbrock 1987). We propose that this broad feature is Raman scattered $\text{He II}\lambda 6545$.

The bottom panel of Fig. 1, we show our spectrum of NGC 6790 around $H\beta$ with the exposure time of 7200 s. If Raman scattered He II exists blueward of $H\alpha$, we may expect a similar feature blueward of $H\beta$. Indeed, when Péquignot et al. (1997) reported the operation of He II Raman scattering in NGC 7027, they detected Raman scattered $\text{He II}\lambda 4850$. In this object, Raman scattered $\text{He II}\lambda 4850$ is not blended with other strong emission lines, which is in contrast with Raman $\text{He II}\lambda 6545$ that is severely blended with $[\text{N II}]\lambda 6548$. In the bottom panel of Fig 1, no broad feature around 4850 \AA is detected with a level of any significance. The quite strong and sharp emission feature at 4851 \AA

is an emission line totally irrelevant with Raman scattering. Aller et al. (1996) identified this emission line as a forbidden line from Fe II. Our spectrum is of insufficient quality to confirm the existence of Raman scattered He II λ 4850. However, this does not cast serious doubts of the Raman scattering nature of the 6545 feature, because Raman He II λ 4850 is always weaker than Raman He II λ 6545. More discussion on this point is presented in section 3.2.

2.2. Line Fitting Analysis

Single Gaussian functions in the form $f(\lambda) = f_0 \exp[-(\lambda - \lambda_c)^2/\Delta\lambda^2]$ are used to fit the permitted emission lines of H α , He II λ 6560, He II λ 6527 and the two N II forbidden lines. The least chi square method is adopted to obtain the best fitting Gaussian functions. We use the atomic spectral data from the website of the National Institute of Standard and Technology (NIST), from which we note that each emission line in our spectra of NGC 6790 appears systematically redward of atomic line center by an amount of 20.7 km s⁻¹. In Table 1, we summarize the result of our profile analysis. The fitting parameters are quite similar to those found for IC 5117 by Lee et al. (2006).

Fig. 2 illustrates our line fitting analysis of the emission lines in NGC 6790. The top panels show the result for H α and He II λ 6560. The short exposure data are used for the H α emission line, which is excellently fitted by a single Gaussian function with a width $\Delta\lambda = 0.54 \text{ \AA}$. He II λ 6560 is also well fitted by a single Gaussian function with a considerably smaller width of $\Delta\lambda = 0.48 \text{ \AA}$ than that for H α .

The middle panels of Fig. 2 show our result for He II λ 6527, which is significantly weak compared with He II λ 6560. He II λ 6527 is strongly blended with another unidentified emission line. Because He II λ 6560 is well-fitted by a single Gaussian, He II λ 6527 should be

also fitted by a single Gaussian function, which is shown by the dotted line in panel (c). The long dashed line in panel (c) shows our Gaussian fit to the unidentified emission line. Groves et al.(2002) noted the existence of [N II] λ 6527 redward of He II λ 6527 with the wavelength difference of 0.14 Å in their spectrum of NGC 6302. However, the unidentified emission line in our spectrum of NGC 6790 can not be [N II] λ 6527, because it appears redward of He II λ 6527 by 1 Å. Furthermore, based on the NIST data, [N II] λ 6527 has the Einstein A coefficient $A = 5.45 \times 10^{-7} s^{-1}$. Compared with [N II] λ 6548 having $A = 9.19 \times 10^{-4}$, [N II] λ 6527 should be weaker than [N II] λ 6548 by a factor of 1700. Based on these atomic data, we plotted [N II] λ 6527 with a dot-dashed line in Fig.2. As is shown in the figure, [N II] λ 6527 is significantly weaker than He II λ 6527, and hence can not affect the over all line fitting result. The 6528Å feature is much stronger than [N II] λ 6527 and still remains to be identified. Panel (d) shows the composite profiles of the two single Gaussian functions in panel (c). From our profile analysis shown also in Table 1, we conclude that the flux ratio of He II λ 6527 and He II λ 6560 is

$$F_{6527}/F_{6560} = 4.1 \times 10^{-2}. \quad (1)$$

The bottom panels of Fig. 2 show the detailed profiles of [N II] lines. It is interesting to note that [N II] λ 6548 exhibits a sharp absorption feature centered at 6548.60 Å. The line center of [N II] λ 6548 appears at 6548.51 Å, and the sharp absorption feature is excellently fitted by a single Gaussian function with a width of $\Delta\lambda = 0.1$ Å and center at $\lambda_0 = 6548.60$ Å. We find no such absorption feature in [N II] λ 6583, which should exhibit exactly the same profile with 3 times more flux (e.g. Osterbrock 1987). To our knowledge, no plausible metal transition is responsible for this sharp absorption. We also checked the telluric absorption lines without finding any strong candidate. In the spectrum of IC 5117 obtained with the 3.6 m Canada-France-Hawaii Telescope we find no similar absorption feature, for which [N II] λ 6548 exhibits exactly the same profile as [N II] λ 6583.

We tentatively propose that this is attributed to $H\alpha$ that is redshifted by an amount of $v_{abs} \sim 800 \text{ km s}^{-1}$. However, in this work, we limit our attention to the Raman scattered He II $\lambda 6545$ with no further discussion of this possibly interesting feature.

Lee et al.(2001) performed a line profile analysis of Raman scattered He II $\lambda 6545$ in a number of symbiotic stars. They subtracted one third of the flux near [N II] $\lambda 6583$ from the flux near [N II] $\lambda 6548$ to expose a broad Raman scattering line feature successfully. However, in view of the existence of the unidentified absorption feature in [N II] $\lambda 6548$ and more severe blending with [N II] $\lambda 6548$, we took another approach, in which the Raman scattered He II $\lambda 6545$ feature is directly fitted from our Monte Carlo data.

3. Monte Carlo Radiative Transfer

3.1. Monte Carlo Procedure

In this subsection, we describe the procedure of our Monte Carlo analysis of the Raman scattered He II $\lambda 6545$. Many planetary nebulae exhibit nonspherical morphology, which may have its origin in the asymmetric mass loss processes. In the case of NGC 6790, the HST image obtained by Kwok et al. (2003) shows elongated shells around the central star. As a first approximation, we adopt a cylindrical shell model for neutral material, which is schematically illustrated in Fig. 3. A similar geometry was considered in the analysis of IC 5117 by Lee et al. (2006).

In this cylindrical shell geometry, the hot UV source is located at the center and H I material is uniformly distributed inside the cylindrical shell with finite height and thickness. The same geometry was adopted by Lee et al. (2006). However, the essential difference is that we now consider the scattering region is expanding with the constant expansion velocity v_{exp} . The cylindrical region is characterized by a uniform H I density n_H , the

height H and the inner and outer radii R_H and $R_H + \Delta R$, respectively. In this case, the H I column density of the cylindrical shell is given by $N_{HI} = n_H \Delta R$.

Since the shell is of uniform density, instead of the physical length l we measure the distance inside the shell in terms of the scattering optical depth τ defined by

$$\tau = n_H \sigma_{tot} l, \quad (2)$$

where σ_{tot} is the sum of the cross sections for Rayleigh and Raman scattering. Since σ_{tot} is a sensitive function of a wavelength of the photon being considered, a given distance may correspond to different optical depths dependent on the wavelength. Therefore, once a photon is generated in the Monte Carlo simulation, we assume that the wavelength does not change as long as it is Rayleigh scattered. Considering that the scattering region is neutral, this assumption should be reasonable.

The basic atomic physics of Raman scattering adopted in our Monte Carlo code is explained in detail by Jung & Lee (2004a). Due to the proximity of He II λ 1025 to H I Ly β resonance, the scattering cross section increases steeply near Ly β . Yoo, Bak & Lee (2002) showed that the branching ratio r_b into Raman scattering increases approximately linearly with wavelength, which is given by

$$\begin{aligned} r_b &= \sigma_{Ram} / \sigma_{tot} \\ &= 0.1342 + 12.50(\lambda - \lambda_{Ly\beta}) / \lambda_{Ly\beta}, \end{aligned} \quad (3)$$

where σ_{Ram} is the cross section for Raman scattering and $\lambda_{Ly\beta}$ is the Ly β center wavelength. Therefore, the Raman conversion into the optical region is quite sensitive to the incident wavelength, which in turn depends on the expansion velocity.

From the energy conservation, a Raman scattered He II feature is characterized by its large width given by

$$\frac{\Delta \lambda_{Ram}}{\lambda_{Ram}} = \left(\frac{\lambda_{Ram}}{\lambda_i} \right) \frac{\Delta \lambda_i}{\lambda_i}, \quad (4)$$

where λ_i and λ_{Ram} are wavelengths of the incident and Raman scattered radiation (e.g. Schmid 1989, Nussbaumer et al. 1989). In the case of Raman He II $\lambda 6545$, the profile width becomes about 6 times broader than He II $\lambda 1025$, which endows a unique property that the profile is mainly determined from the relative motion between the emitter and the scatterer.

In our Monte Carlo calculation, we also consider the re-entry of a photon emerging from the inner wall of the cylinder, for which we assume that this photon travel freely until it hits the inner wall on the opposite side. We consider a photon with a unit wavevector $\hat{\mathbf{k}}$ supposed to travel a scattering optical depth τ from the position $\mathbf{r}_i = (x_i, y_i, z_i)$. If this photon emerges from the inner wall of the cylinder, we find the two points of intersection with the inner wall of the cylinder. This is accomplished by solving the quadratic for τ_p

$$R_H^2 = |(\mathbf{r}_i + \tau_p \hat{\mathbf{k}}) \cdot \hat{\rho}|^2, \quad (5)$$

for which we denote the two solutions by τ_{p1} and τ_{p2} with $\tau_{p2} > \tau_{p1}$. Here, $\hat{\rho}$ is the unit vector pointing radially outward from the cylinder axis. The difference of the two solutions $\Delta\tau_p$ is given by

$$\begin{aligned} \Delta\tau_p &= \tau_{p2} - \tau_{p1} \\ &= \frac{2\sqrt{R_H^2(1 - k_z^2) - (k_x y_i - k_y x_i)^2}}{(1 - k_z^2)}, \end{aligned} \quad (6)$$

where k_x, k_y and k_z are the components of $\hat{\mathbf{k}}$. By adding $\Delta\tau_p$ to the original photon path, we find the new scattering site in the other side of the shell.

The incident He II $\lambda 1025$ line flux and profile can be inferred from the case B recombination theory of single electron atoms provided by Storey & Hummer (1995). In Table 2, we show the expected He II $\lambda 1025$ line flux relative to He II $\lambda 6560$ and He II $\lambda 6527$ for electron number densities $n_e = 10^4, 10^6$ and 10^8 cm^{-3} and temperatures $T_e = 10^4$ and $2 \times 10^4 \text{ K}$. We note that our observed flux ratio of He II $\lambda 6527$ and He II $\lambda 6560$ given in Eq. (1) is consistent with the nebular condition of $n_e \sim 10^6 \text{ cm}^{-3}$ and $T_e = 10^4 \text{ K}$.

However, this choice is not unique and the range of He II λ 1025 is already quite significant with the choice of parameters in Table 2. With this caveat in mind, we fix the electron number density $n_e = 10^6 \text{ cm}^{-3}$ and $T_e = 10^4 \text{ K}$. Adopting these values of n_e and T_e , the recombination theory by Storey & Hummer (1995) gives $F_{1025} = 4.2F_{6560}$, which is used for our Monte Carlo calculations.

The Monte Carlo simulation starts with a generation of He II λ 1025 line photons having the same line profile with that of observed He II λ 6560, and appropriately scaled using the recombination theory. As He II λ 6560 is fitted by a single Gaussian with a width of $\Delta\lambda = 0.48 \text{ \AA}$, we note that the line profile function f_{UV} for He II λ 1025 is given by

$$f_{UV}(\lambda) = f_{1025} \exp -[(\lambda - \lambda_{1025})^2 / \Delta\lambda_{1025}^2] \quad (7)$$

with $\Delta\lambda_{1025} = 0.48 \cdot 1025/6560 \text{ \AA} = 0.075 \text{ \AA}$. Here, the peak value f_{1025} is appropriately adjusted to yield $F_{1025} = 4.2F_{6560}$.

We trace each individual He II λ 1025 line photon until it escapes from the H I region. From Eq. (4), it is noted that the profiles of the Raman scattered features are determined from the relative kinematics between the emission source and the H I region and almost independent of the observer’s line of sight. Therefore, in this work, we collect all the photons irrespective of the final direction.

3.2. Simulated Raman Profiles

3.2.1. Spherical Emission Region

In the work of Lee et al. (2006), the analysis of Raman scattered He II λ 6545 was purely based on the atomic physics and focused on the exact location of line center. Their computation shows that the Raman scattered feature should be centered significantly

blueward of [N II] λ 6548. In Fig. 1, we note that the Raman He II λ 6545 is completely blended with [N II] λ 6548, which implies that the neutral scattering region should be receding from the central UV source.

In Fig. 4, we show our Monte Carlo profiles for various expansion speeds v_{exp} of the neutral scattering region with respect to the hot central star. In this figure, the height of the cylinder is taken to be infinite so that the covering factor of the scattering region is unity. The column density is fixed to $N_{HI} = 1 \times 10^{20} \text{ cm}^{-2}$. The solid line shows our observed data and the other lines show our Monte Carlo profiles corresponding to various values of v_{exp} . We can clearly notice the center shift of the Raman He II λ 6545, which is highly enhanced due to the line broadening given in Eq. (4). The top panel shows the profiles for velocities $v_{exp} \leq 40 \text{ km s}^{-1}$. The bottom panel shows the profiles for velocities in the smaller range $14 \text{ km s}^{-1} \leq v_{exp} \leq 22 \text{ km s}^{-1}$. From the figure, the plausible expansion velocity is around 20 km s^{-1} , for which the peak wavelength resides inside the [NII] λ 6548 emission line.

One interesting point to note from Fig. 4 is that the strength of the Raman feature increases sharply as v_{exp} increases despite the fact that the covering factor and N_{HI} are fixed. This is explained by the fact that the Raman scattering cross section sharply increases near H α due to Ly β resonance in the parent wavelength space. Therefore, a receding H I region yields more Raman scattered He II λ 6545 photons than when the same region is stationary. This complicated dependence of the scattering cross section on wavelength also results in slightly asymmetric Raman profiles, which is barely noticeable in Fig. 4. Therefore, the Raman conversion efficiency may be estimated accurately only after the kinematics of the scattering region with respect to the emission source is carefully determined.

In the left panel of Fig. 5, we show the Raman profiles for various H I column densities ranging $N_{HI} = 10^{19} - 1.5 \times 10^{20} \text{ cm}^{-2}$ with the fixed values of $H/R_H = 2$ and $v_{exp} = 20 \text{ km s}^{-1}$. Within this range of N_{HI} , the overall strength is nearly proportional

to the H I column density, because the H I region is mostly optically thin with respect to Raman scattering of He II λ 1025. This expansion speed is very similar to the value of 16 km s⁻¹ determined from Doppler shifted Na D absorption lines by Dinerstein, Sneden & Uglum (1995).

The right panel of Fig. 5 shows the Monte Carlo Raman profiles for various covering factors of the cylindrical shell. As is expected, the overall strength is also proportional to the covering factor. In both the panels of Fig. 5, we obtain qualitatively similar profiles. This implies that the Raman profile analysis severely suffers from the degeneracy problem involving the covering factor and H I column density.

With this caveat in mind related with the degeneracy in N_{HI} and the covering factor, we show our best fit profile from the Monte Carlo calculations in Fig. 6. The model parameters are $v_{exp} = 19$ km s⁻¹, $N_{HI} = 9 \times 10^{19}$ cm⁻² and $H/R_H = 1.7$. As in IC 5117, the H I region significantly covers the hot central star in NGC 6790. However, in this figure we notice that the model profiles exhibit deficit both in the blue wing and red wing parts. If this deficit is real, then it implies that in the direction to the H I region the incident profile is broader than in the observer’s line of sight. The next subsection discusses this point.

Jung & Lee (2004b) developed a Monte Carlo code to compute the line profile of Raman scattered He II 4850 and analyzed their spectrum of the symbiotic star V1016 Cyg. Using the same code, we show in Fig. 7 the Monte Carlo profile for Raman scattered He II 4850 by a long dashed line. The same column density and covering factor as in Fig. 6 were used in this calculation. In the figure, the solid line shows the BOES data with the exposure time of 7200 s. Our observational data are barely consistent with our interpretation of Raman scattering nature. The poor quality of the current observational data hinders a further serious quantitative analysis. A more fruitful analysis may be made only after observational data with a better quality are secured.

3.2.2. *Ring-like Emission Region*

In this subsection, we perform line profile analyses in the case where the emission region takes the form of a ring that is rotating in the vicinity of the hot central star. In the previous section, it was assumed that the He II emission region is spherically symmetric and stationary. However, it is highly probable that the distribution of nebular material significantly deviates from spherical symmetry considering the non-spherical shape exhibited by most planetary nebulae (e.g. Corradi & Schwarz 1995). In this case, the emission region may plausibly possess an ordered motion component, which may also be associated with the nonspherical nebular morphology. Therefore, we may expect that ionized material is concentrated on the equatorial plane having some slow rotation velocity component.

There exists little kinematic information available on the emission region very near the central star. No observational data of NGC 6790 are available in the archives of HUT and FUSE. In consideration of the absence of a unique kinematic model accounting for all the observed emission line profiles, we adopt a simple ring-like emission region, in which we investigate the line of sight effect on the profiles of the He II emission and Raman scattered lines. Depending on the line of sight of the observer, the rotation velocity component is reduced by the factor $\sin i$, where i is the inclination angle of the ring. However, Eq. (4) dictates that the Raman profile is determined by the velocity component of the emitter with respect to the scatterer and fairly insensitive to the line of sight.

This proposition leads to an interesting interpretation of our profile fitting of $H\alpha$ and He II $\lambda 6560$ presented in the previous section. We may decompose the emission profiles into a bulk component and a random component. We further assume that the bulk component represents a slow rotation in the equatorial plane and that the random component is attributed to a thermal motion and a turbulent motion. For the sake of simplicity, we assume that He II $\lambda 6560$ and $H\alpha$ are formed in the same ring-like region that is in slow

rotation in the equatorial plane with the speed v_{bulk} .

A He ion being 4 times heavier than a hydrogen nucleus, the line width of He II due to the thermal motion is half of that for H α if they are formed in the same region. However, if the emission region possesses some turbulent component, then overall random motion component for hydrogen is broader than that of He II by a factor less than 2. If we denote the electron temperature of NGC 6790 by $T_e = 10^4 T_4$ K, then the thermal velocity associated with H α is given by

$$v_{th,H} = \sqrt{\frac{k_B T_e}{2m_p}} = 13 T_4^{1/2} \text{ km s}^{-1}, \quad (8)$$

where m_p is the proton mass and k_B is the Boltzmann constant (e.g. Rybicki & Lightman 1979). Introducing v_{turb} for the turbulent velocity scale, we denote the random velocity components of H α and He II λ 6560 by $v_{ran,H}$ and $v_{ran,He}$, respectively, where

$$\begin{aligned} v_{ran,H} &= v_{turb} + v_{th,H} \\ v_{ran,He} &= v_{turb} + (v_{th,H}/2). \end{aligned} \quad (9)$$

Noting that there are three model parameters, namely i , v_{bulk} and v_{turb} for the two line widths, we also encounter a degeneracy problem. Hoping that future observations may provide independent constraints on some of these model parameters, we just pick out a set of values that yield a reasonable fit to our observed data. In the top panels of Fig. 8, we show model line profiles for He II λ 6560 and H α from one such set consisting of

$$\begin{aligned} \sin i &= 0.6, \quad v_{bulk} = 18 \text{ km s}^{-1}, \quad v_{turb} = 14 \text{ km s}^{-1}, \\ v_{th,H} &= 14 \text{ km s}^{-1}, \quad v_{th,He} = 0.5v_{th,H}. \end{aligned} \quad (10)$$

The thermal velocity $v_{th,H} = 14 \text{ km s}^{-1}$ is consistent with the electron temperature $T_e = 10^4$ K, which is similar to that obtained by Aller et al. (1996) from their photoionization modeling. The overall fits to both H α and He II λ 6560 appear quite good.

The bulk velocity component is consistent with the size of the emission ring region of order 1 AU if we interpret the bulk motion to be Keplerian. However, the bulk motion may not be related with the Keplerian motion but may be related with the rotation component of the central star, for which case the physical size of the emission region can be at best poorly constrained.

Because the H I region is also concentrated on the equatorial plane, the full bulk velocity component should be considered without the inclination effect for far UV He II $\lambda 1025$ that is incident on the H I region. In the bottom panel of Fig 8, the dotted line shows the He II $\lambda 6560$ profile that would be measured by a hypothetical observer in the equatorial plane. It is excellently fitted by a single Gaussian function with a width $\Delta\lambda = 0.61 \text{ \AA}$, which is significantly larger than the observed value of $\Delta\lambda = 0.48 \text{ \AA}$ by a factor of 1.3. Hence, the emission profile for He $\lambda 1025$ incident on the neutral region should also be broadened by the same factor.

In Fig. 9, we show our Monte Carlo result using the profile shown in the bottom panel of Fig. 8 and appropriately scaled to He II $\lambda 1025$. The other model parameters are also adjusted for better fit and they are $v_{exp} = 15 \text{ km s}^{-1}$, $N_{HI} = 9 \times 10^{19} \text{ cm}^{-2}$ and $H/R_H = 1.2$. A much better fit is obtained than that considered in the previous section. However, it should also be pointed out that in constructing the profile in Fig. 9 more model parameters have been used than in the previous section and still the degenerate nature of the problem persists.

The expansion velocity of the H I shell in Fig. 9 is only $v_{exp} = 15 \text{ km s}^{-1}$, which is significantly smaller than the value $v_{exp} = 19 \text{ km s}^{-1}$ presented in Fig. 6. This notable discrepancy in expansion velocity is attributed to the scattering cross section that is sharply peaked around $H\alpha$. According to Jung & Lee (2004a), this leads to the center shift of a Raman scattered He II feature, which is dependent on the column density. The result shown

in Fig. 9 implies that the shape or the width of the incident profile also affects the location of the line center. A more quantitative investigation in a significantly large parameter space is left to the future work.

4. Discussion

H I Raman spectroscopy provides an accurate determination of the expansion velocity of the H I region, for the measurement of which H I 21 cm radio observation has been the unique tool so far. Our analysis shows that the expansion velocity lies between 15 km s^{-1} and 19 km s^{-1} , which is consistent with the value of 16 km s^{-1} provided by Taylor et al. (1990). As was pointed out by Lee et al. (2006) the Raman spectroscopy allows one to determine the H I column density whereas the excitation temperature should be assumed before N_{HI} is deduced from H I 21 cm radio observation. According to Taylor et al. (1990), $N_{HI} = 2.7 \times 10^{20} \text{ cm}^{-2}$ assuming the excitation temperature $T_{HI} = 100 \text{ K}$. Our Raman profile analysis lends support to this excitation temperature.

Our current data are of insufficient quality to lift the degeneracy of the covering factor and H I column density, and the overall strength of the Raman feature is determined from the product of the two quantities. However, our Monte Carlo calculations show that Raman profiles exhibit redward asymmetry due to enhanced scattering cross section toward $H\alpha$ resonance. With better quality spectra that may be available from bigger telescopes, it is hoped that tighter constraints are obtained from more refined profile analyses. If Raman scattered He II 4850 blueward of $H\beta$ can also be used, additional constraints can be put to break the degeneracy.

Even though the distance to NGC 6790 is highly uncertain, we may assume that the distance is about 1 kpc for simple order of magnitude calculations. According to Tyllenda

et al. (2003), the angular size of NGC 6790 is $\sim 3''$. This gives a physical size of the H I region $R \sim 5 \times 10^{16}$ cm. If the H I region is of a thin cylindrical shell with the height similar to its radius, the total number N_{tot} of hydrogen atoms inside the shell is approximately given by $N_{tot} = 2\pi R^2 N_{HI} \sim 6 \times 10^{54}$. Here, in our order of magnitude estimate, we ignore the inclination effect, which will overestimate the total number of hydrogen atoms by the factor $\sin i$. The H I mass of the neutral region is inferred to be $M_{HI} \sim 4 \times 10^{-3} M_{\odot}$.

Furthermore, the expansion velocity of $v_{exp} \sim 15$ km s $^{-1}$ and the physical size of $R \sim 5 \times 10^{16}$ cm together imply the age of order of a thousand years for NGC 6790. It should be pointed out that these rough calculations are highly dependent on the assumed distance to NGC 6790 and still the physical size of the H I region is quite uncertain.

The origin of sharp absorption feature that appeared in [N II] λ 6548 is quite uncertain. If this absorption feature is attributed to H α , then it may imply the existence of clumpy components having a small covering factor with respect to the [N II] emission region and receding with a significant velocity of ~ 800 km s $^{-1}$. In some planetary nebulae including M2-9 and NGC 6543, it is known that fast collimated outflows exist around the central star with a velocity of order 1000 km s $^{-1}$ (Balick 1989, Gruendl, Chu & Guerrero 2004, Prinja et al. 2007). Ueta, Fong & Meixner (2001) presented near IR imaging observations of AFGL 618 and reported their findings of molecular bullet-like features moving faster than 200 km s $^{-1}$. However, it still remains a mystery whether a clumpy bullet-like object can be ejected with so large a velocity from the center region.

It should be pointed out that a ring-like emission model may not be a unique choice for the observed profiles of He II λ 6560 and H α . Many kinematical models involving jet-like outflows or radial infall and/or outflows may also yield similarly well-fitting profiles. Therefore without convincing support from other studies such as imaging observations using interferometry or hydrodynamical computations, it appears to be too early to conclude

about the kinematics of the He II emission region.

A ring-like emission region and H I region concentrated in the equatorial region may provide interesting opportunities for spectropolarimetry. In symbiotic stars, Raman scattered O VI $\lambda\lambda 6825, 7088$ are known to exhibit strong linear polarization (e.g. Harries & Howarth 1996, Schmid 1998). The polarization structure may be closely related with the accretion and mass loss processes that deviate from spherical symmetry (e.g. Lee & Park 1999, Lee & Kang 2007, Ikeda et al. 2004). Because Raman scattered features consist of purely scattered photons, they make ideal targets for linear spectropolarimetry. Future spectropolarimetric studies may provide more interesting information regarding the mass loss processes in AGB stars and planetary nebulae.

We are grateful to the staffs at the Bohyunsan Optical Astronomy Observatory. We also thank an anonymous referee for the constructive comments, which significantly improved the presentation of our work. This research was supported by the Astrophysical Research Center for the Structure and Evolution of the Cosmos (ARCSEC”) funded by the Korea Science and Engineering Foundation.

REFERENCES

- Aller, L. H., Hyung, S. & Feibelman, W., A., 1996, *PASP*, 108, 488
- Altschuler, D. R., Schneider, S. E., Giovanardi, C., & Silverglate, P. R., 1986, *ApJ*, 305, L85
- Balick, B., 1989, *AJ*, 97, 476
- Birriel, J. J., 2004, *ApJ*, 612, 1136
- Corradi, R. & Schwarz, H. E., 1995, *A&A*, 293, 871
- Dinerstein, H. L., Sneden, C., & Uglum, J., 1995, *ApJ*, 447, 262
- Espey, B. R., Schulte-Ladbeck, R. E., Kriss, G. A., Hamann, F., Schmid, H. M., Johnson, J. J., 1995, *ApJ*, 454, L61
- Gathier, R., Pottasch, S. R. & Goss, W. M., 1986, *A&A*, 157, 191
- Groves, B., Dopita, M. A., Williams, R. E., & Hua, C. -T., 2002, *PASA*, 19, 425
- Gruendl, R. A., Chu, Y.-H., Guerrero, M. A., *ApJ*, 617, L127
- Gussie, G. T., & Taylor, A. R., 1995, *MNRAS*, 273, 801
- Harries, T. J., & Howarth, I. D., 1996, *A&AS*, 119, 61
- Ikeda, Y., Akitaya, H., Matsuda, K., Homma, K., Seki, M., Kawabata, K. S., Hirata, R., Okazaki, A., 2004, *ApJ*, 604, 357
- Jung, Y. -C., & Lee, H. -W., 2004a, *MNRAS*, 350, 580
- Jung, Y. -C., & Lee, H. -W., 2004b, *MNRAS*, 355, 221

- Kim, K. -M., Han, I., Valyavin, G. G., Plachinda, S., Jang, J. G., Jang, B. -H., Seong, H. C., Lee, B. -C., Kang, D. -I., Park, B. -G., Yoon, T. S., & Vogt, S. S., 2007, *PASP*, 119, 1052
- Kwok, S., Su, K., Y. L., & Sahai, R., 2003, *IAUS*, 209, 481
- Lee, H. -W., Jung, Y. -C., Song, I. -O. & Ahn, S. -H., 2006, *ApJ*, 636, 1045
- Lee, H. -W., & Kang, S., 2007, *ApJ*, 669, 1156
- Lee, H. -W., Kang, Y. -W., Byun, Y., -I., 2001, *ApJ*, 551, L121
- Lee, H. -W., & Park, M.-G., 1999, *ApJ*, 515, L89
- Nussbaumer, H., Schmid, H. M., & Vogel, M., 1989, *A&A*, 211, L27
- Osterbrock, D., 1987, *Astrophysics of Gaseous Nebulae and Active Galactic Nuclei*, University Science Books, Mill Valley
- Péquignot, D., Baluteau, J. -P., Morisset, C., & Boisson, C., 1997, *A&A*, 323, 217
- Prinja, R. K., Hodges, S. E., Massa, D. L., Fullerton, A. W., Burnley, A. W., 2007, *MNRAS*, 382, 299
- Rybicki, G. B., & Lightman, A. P., 1979, *Radiative Processes in Astrophysics*, John Wiley & Sons, Inc., New York
- Schmid, H. M., 1989, *A&A*, 211, L31
- Schmid, H. M., 1998, *Reviews in Modern Astronomy*, 11, 297
- Schneider, S. E., Silver, P. R., Altschuler, D. R., & Giovanardi, C., 1987, *ApJ*, 314, 572
- Storey, P. J. & Hummer, D. G., 1995, *MNRAS*, 272, 41

Taylor, A. R., Gussie, G. T., & Pottasch, S. R., 1990, ApJ, 351, 515

Tylenda, R., Siódmiak, N., Górny, S. K., Corradi, R. L. M., Schwarz, H. E., 2003, A&A, 405, 627

Ueta, T., Fong, D. & Meixner, M., 2001, ApJ, 557, L117

Van Groningen, E., 1993, MNRAS, 264, 975

Yoo, J. J., Bak, J.-Y., Lee, H. -W., 2002, MNRAS, 336, 467

Zhang, C. Y., 1995, ApJS, 98, 659

This manuscript was prepared with the AAS L^AT_EX macros v5.2.

Table 1. Single Gaussian Fit Parameters of Emission Lines

Line	λ_0 (Å)	f_0	$\Delta\lambda$ (Å)
H α 6563	6563.23	34.8	0.54
He II λ 6560	6560.58	0.072	0.48
He II λ 6527	6527.49	0.00295	0.48
[N II] λ 6548	6548.51	0.897	0.47
[N II] λ 6583	6583.90	2.73	0.48

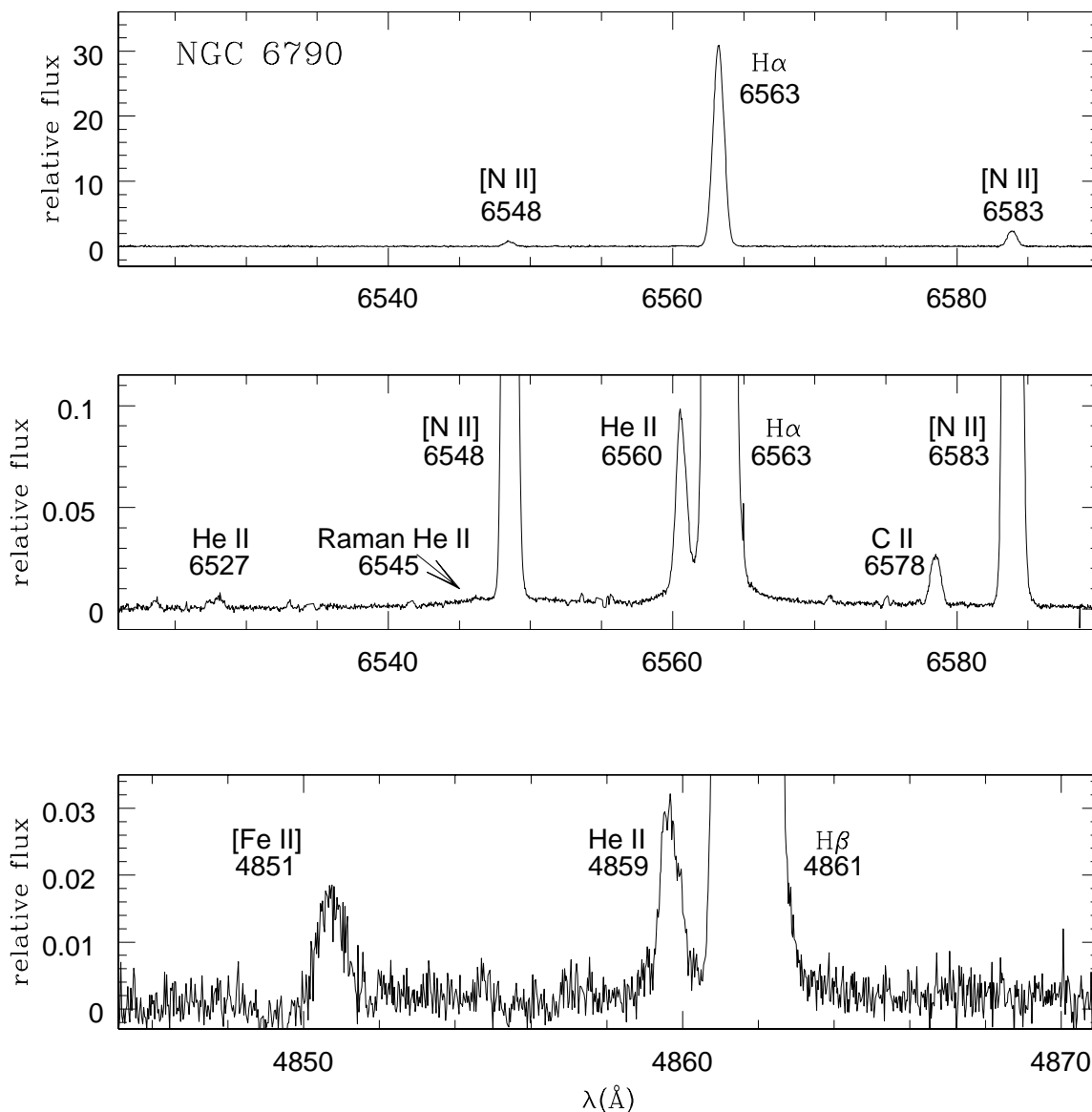


Fig. 1.— High resolution spectra of NGC 6790 obtained with BOES. The top panel is a short exposure spectrum with exposure time of 600 s, and the exposure time for the middle and bottom panels is 7200 s. The relative flux density is normalized such that [N II] λ 6548 has the flux density peak of unity. In the top panel, the strongest emission line H α is unsaturated. We also clearly see [N II] lines at 6548 \AA and 6583 \AA . In the middle panel, we note that around [N II] λ 6548 there exists a broad wing feature. No similar feature is present around 3 times stronger [N II] λ 6583, which means that the broad wing feature around [N II] λ 6548 is not associated with [N II] nor is an instrumental artifacts. The bottom panel shows the H β part of the BOES spectrum. The insufficient quality of the data hinders the clear detection

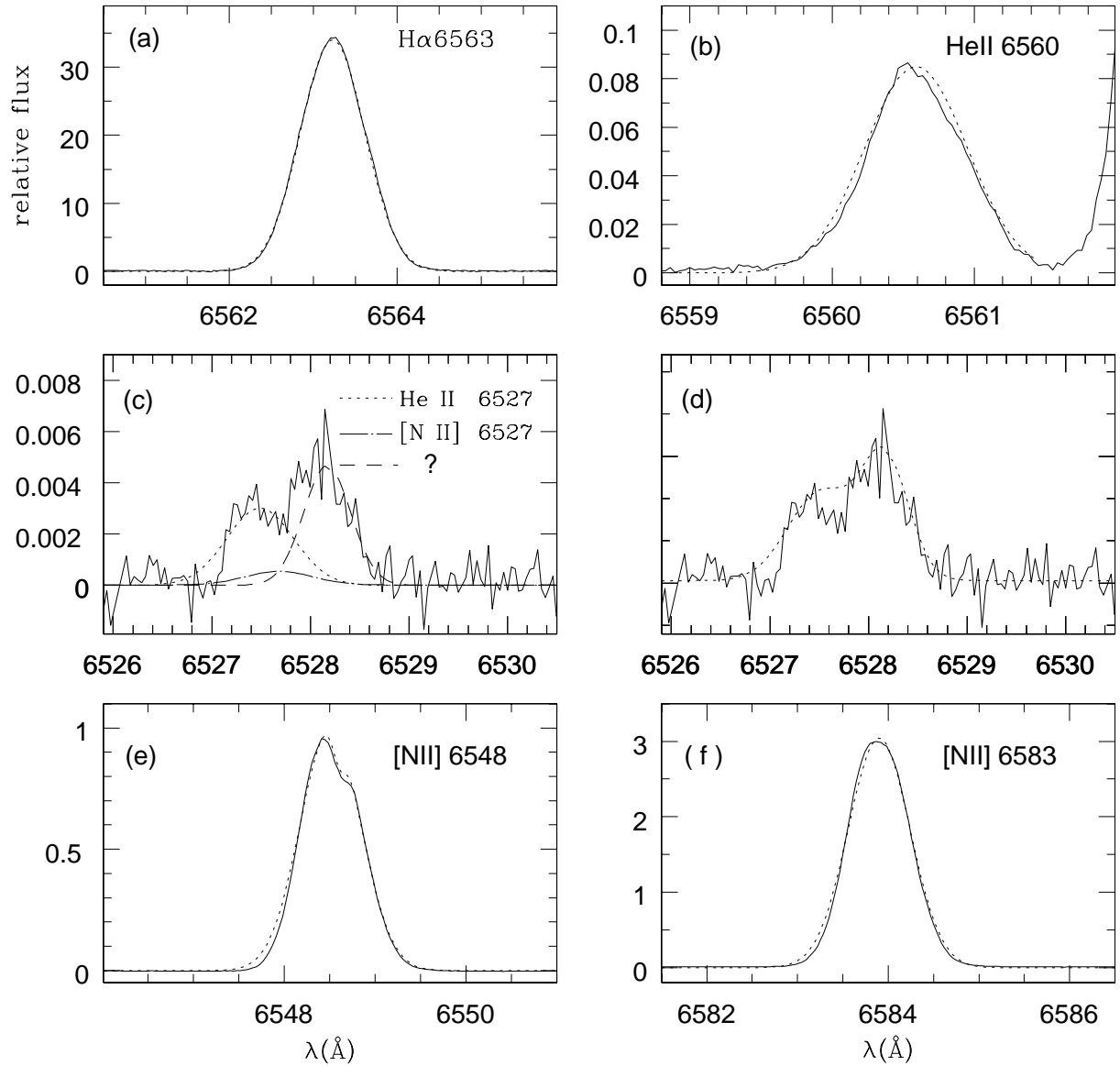


Fig. 2.— Gaussian line fitting analysis. The solid lines show the observational data and the dotted lines show our Gaussian fits. The same flux normalization as in Fig.1 is used. The top panels show the results for $\text{H}\alpha$ and $\text{He II}\lambda 6560$. The middle panels show the line fitting result for $\text{He II}\lambda 6527$ and a nearby unidentified emission line. $\text{He II}\lambda 6527$ is fitted by a single Gaussian function, which is shown by the dotted line in panel (c). The long dashed line in panel (c) shows the unidentified emission line. Using the atomic data provided by NIST, we show the line contribution from $[\text{N II}]\lambda 6527$ by a dot-dashed line. In panel (d) we show the composite profile from the three single Gaussians shown in panel (c). The bottom panels show the detailed views of $[\text{N II}]$ lines. There is a sharp absorption feature in $[\text{N II}]\lambda 6548$

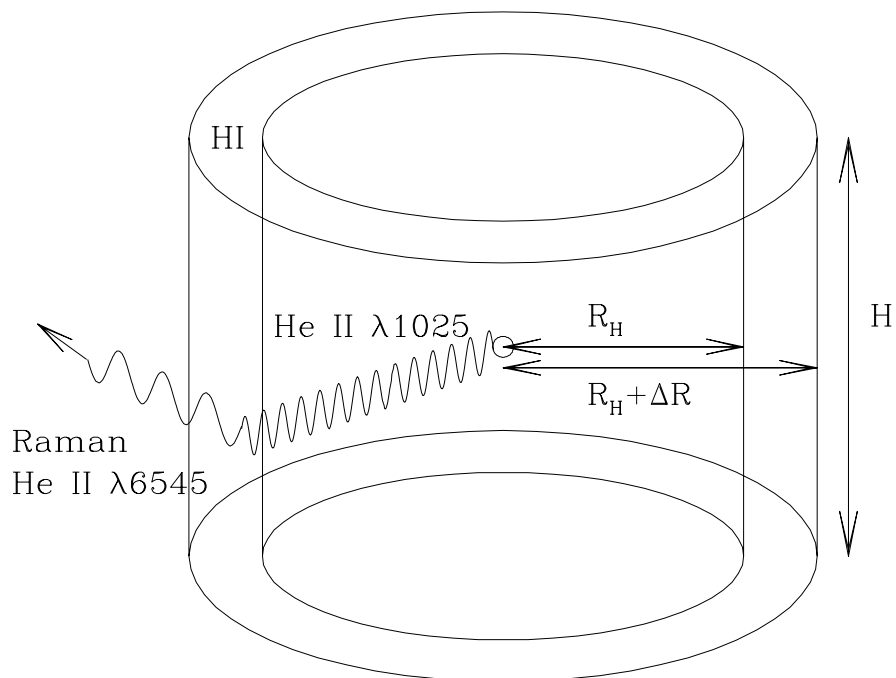


Fig. 3.— A schematic diagram of the Raman scattering geometry adopted in this work. The hot star and He II emission region are located at the center. Surrounding the UV emission region, the H I scattering region takes the form of a cylindrical shell with the inner radius R_H , the outer radius $R_H + \Delta R$ and the height H . In this work, the cylindrical shell is assumed to expand with the speed v_{exp} . Hydrogen atoms are distributed uniformly with a number density n_H inside the cylindrical shell.

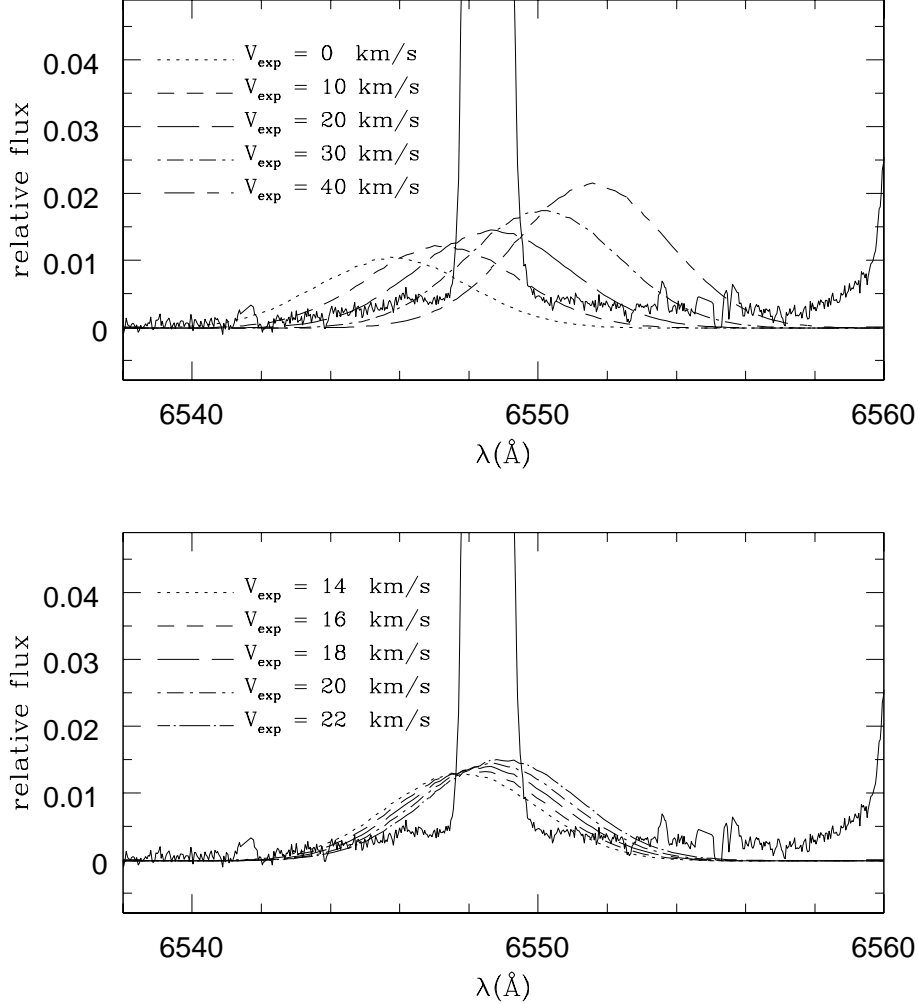


Fig. 4.— Line profiles of Raman scattered He II $\lambda 6545$ from our Monte Carlo simulations for various expansion speeds. The covering factor is fixed to be unity and $N_{HI} = 10^{20} \text{ cm}^{-2}$. Due to the inelasticity of Raman scattering or Eq.(4), the location of line center is fairly sensitive to v_{exp} . The top panel shows the profiles for velocities in the range $v_{\text{exp}} \leq 40 \text{ km s}^{-1}$ in an interval of 10 km s^{-1} . The bottom panel shows the profiles for velocities in the range $14 \text{ km s}^{-1} \leq v_{\text{exp}} \leq 22 \text{ km s}^{-1}$. It is notable that the expansion velocity v_{exp} affects both the location of line center and the total Raman flux.

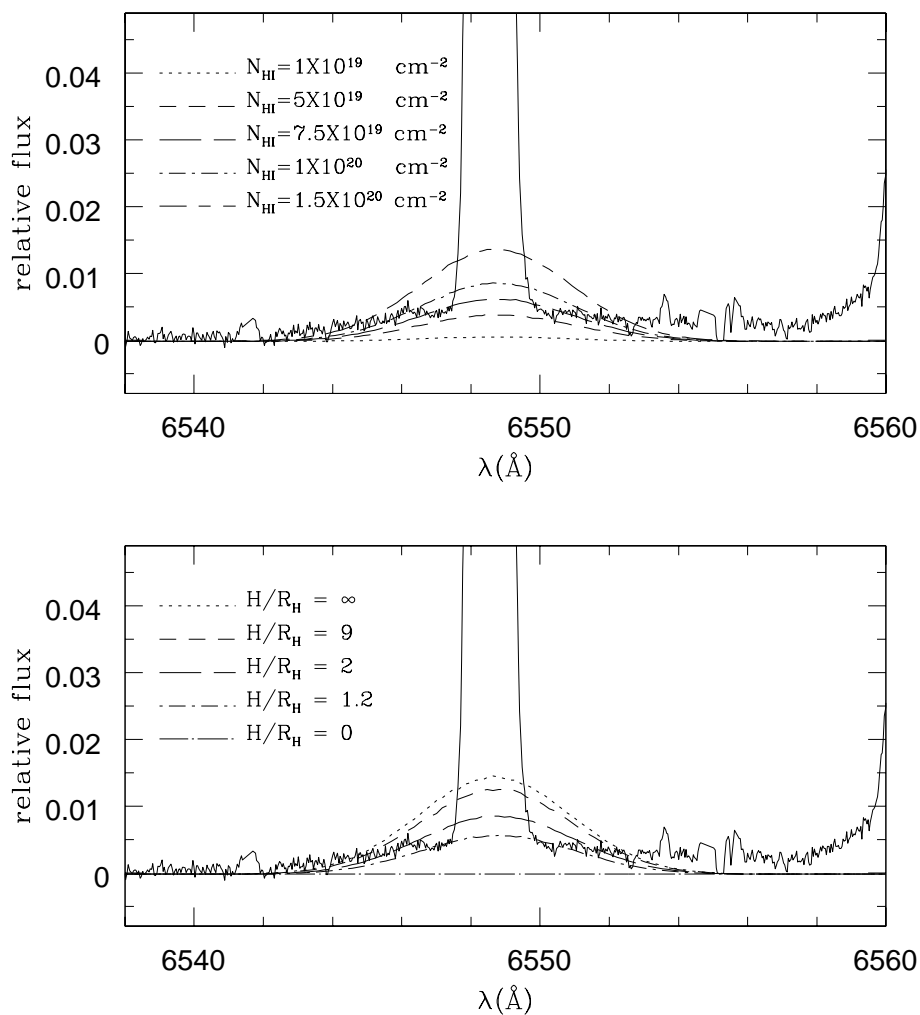


Fig. 5.— Monte Carlo line profiles of Raman scattered He II $\lambda 6545$ for various N_{HI} and covering factors. The left panel shows the Monte Carlo profiles for various N_{HI} with the covering factor fixed to be $H/R_H = 2$. The right panel shows the simulated profiles for various covering factors with fixed $N_{HI} = 10^{20} \text{ cm}^{-2}$.

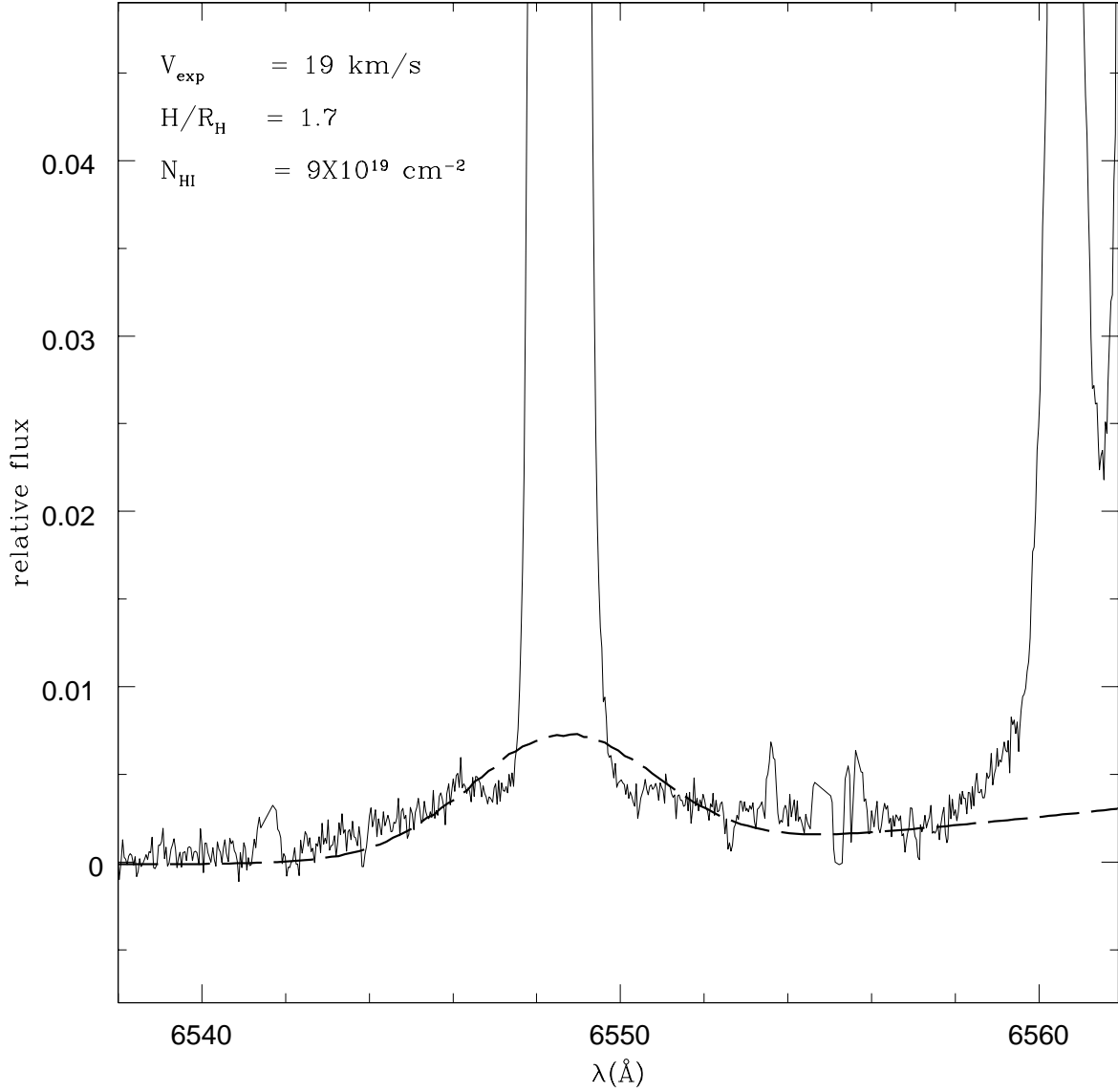


Fig. 6.— Our best fit Monte Carlo profile of Raman scattered He II $\lambda 6545$ from a stationary emission region surrounded by a cylindrical shell. The dotted line is the Monte Carlo line profile and the solid line is the observed data. The adopted parameters are $v_{\text{exp}} = 19 \text{ km s}^{-1}$, $H/R_H = 1.7$, $N_{\text{HI}} = 9 \times 10^{19} \text{ cm}^{-2}$.

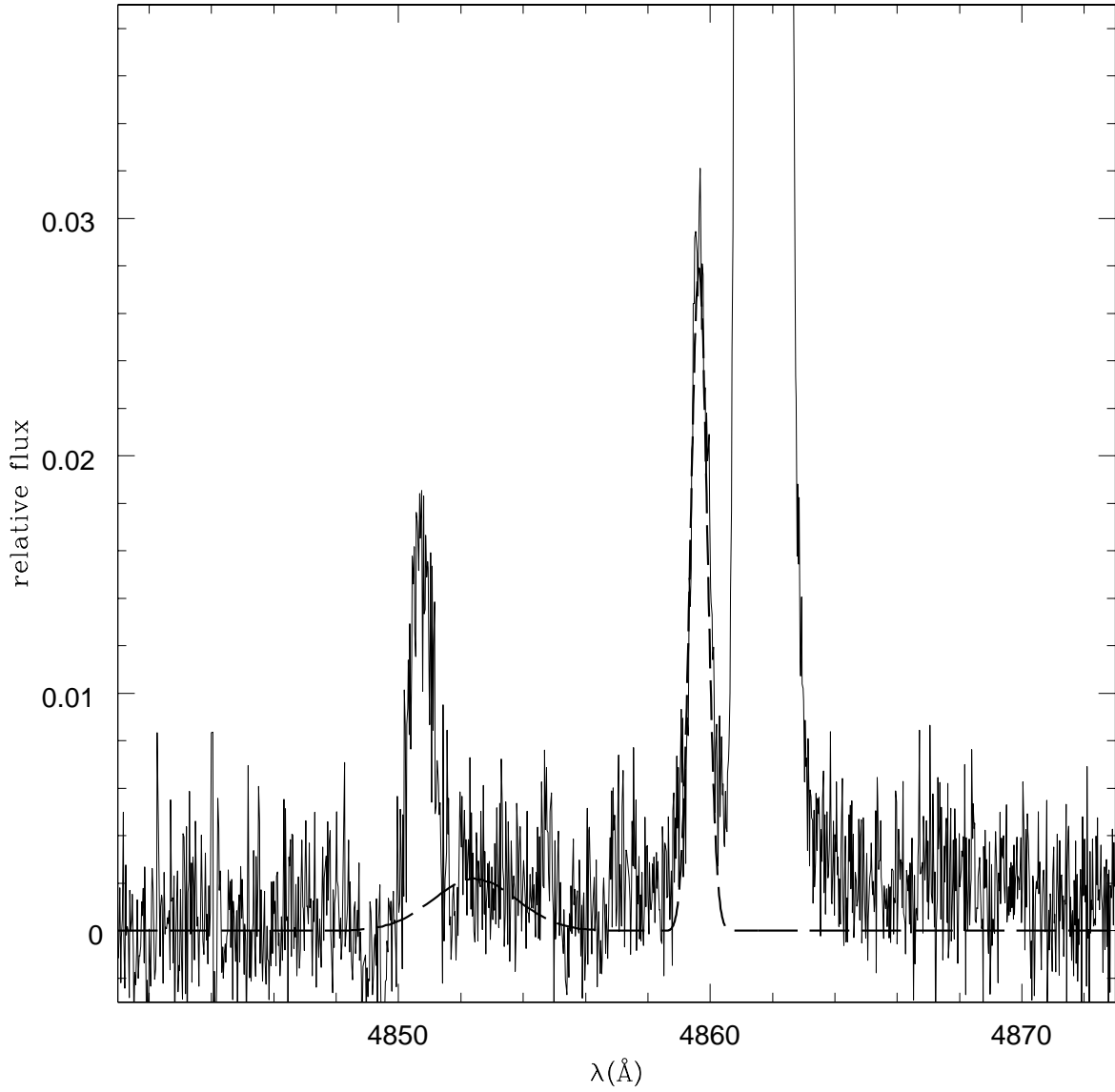


Fig. 7.— BOES data around $H\beta$ (solid line) and the Monte Carlo profile of Raman scattered $He II\lambda 4850$ (long dashed line). The same column density and covering factor as in Fig.6 were used in the Monte Carlo calculation. The observational data are barely consistent with the Monte Carlo result.

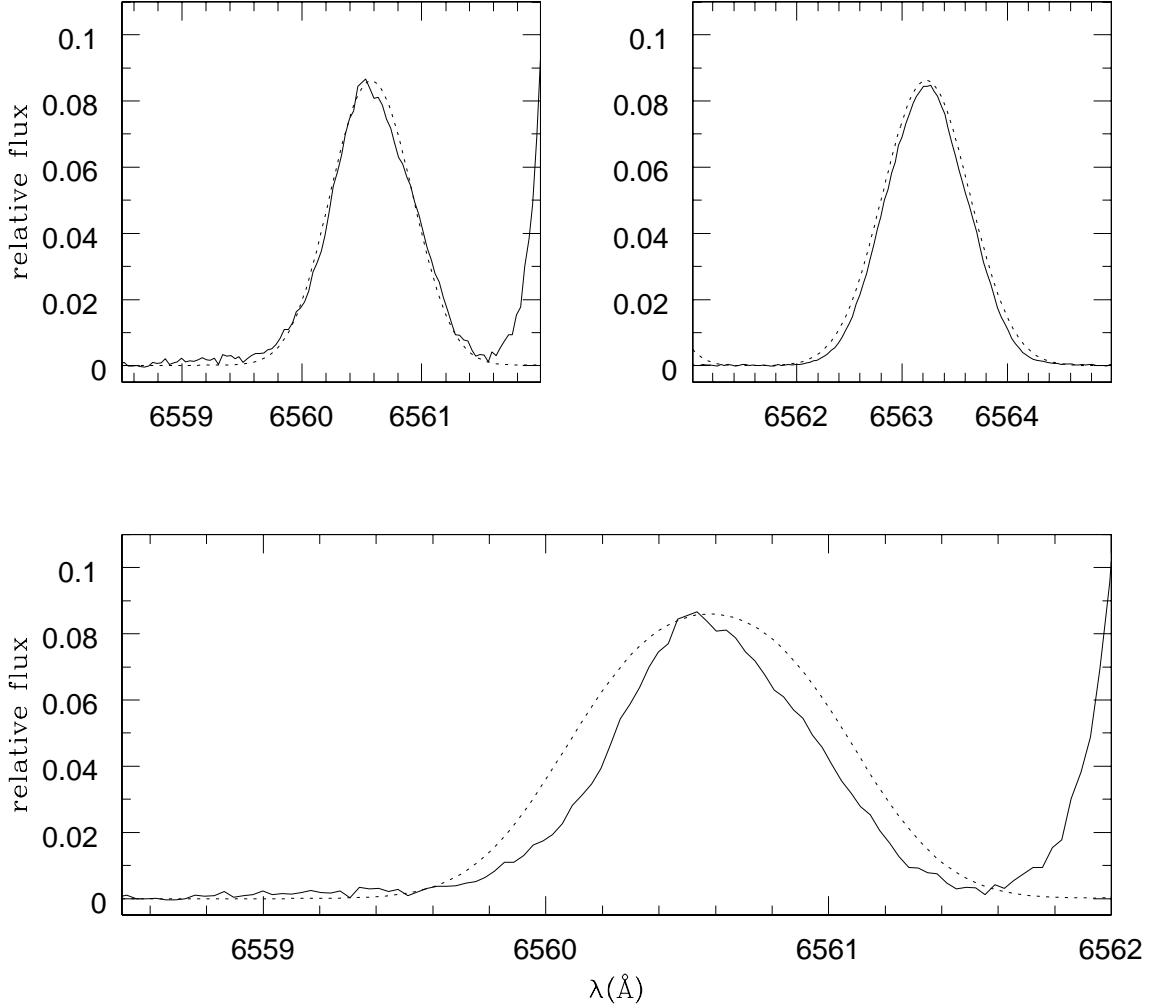


Fig. 8.— Line profiles of He II $\lambda 6560$ and H α from a ring-like emission region. The axis of the ring makes an angle i with the line of sight, where we take $\sin i = 0.6$ as an example. The upper panels show line profiles of He II $\lambda 6560$ and H α viewed from the observer’s line of sight. The fitting parameters are $v_{bulk} = 18 \text{ km s}^{-1}$, $v_{turb} = 14 \text{ km s}^{-1}$ and $v_{th,H} = 14 \text{ km s}^{-1}$, $v_{th,He} = 0.5v_{th,H}$. See the text of the definitions of these velocities. The solid lines represent the BOES data and the dotted lines are model profiles. The lower panel shows the observed He II $\lambda 6560$ profile (solid line) and the model profile that would be observed in the equatorial direction. The dotted model profile is excellently fitted by a single Gaussian with a width $\Delta\lambda = 0.61 \text{ \AA}$

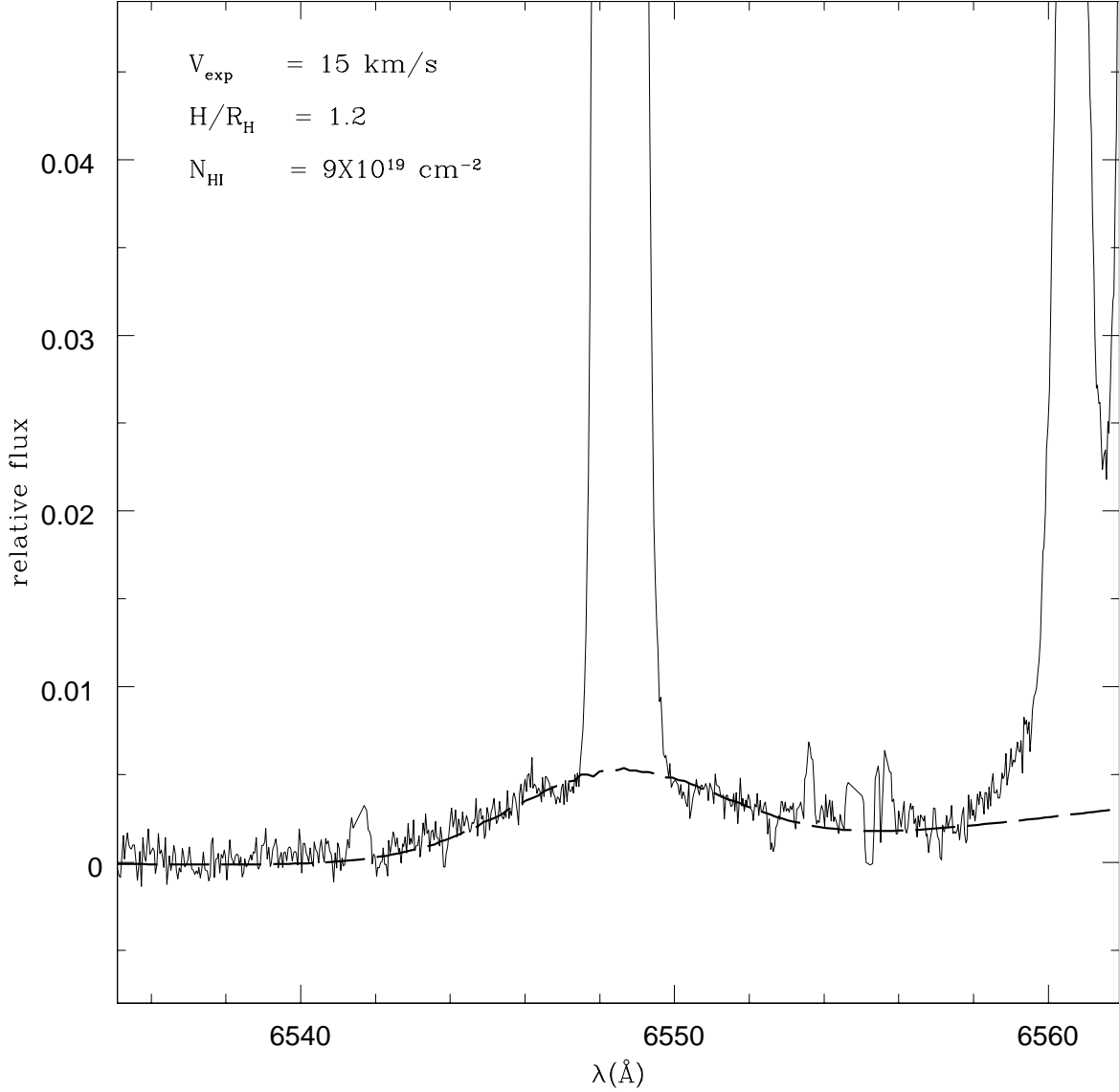


Fig. 9.— A Monte Carlo best fit profile (dotted line) of Raman scattered He II $\lambda 6545$ from a ring-like emission region considered in Fig. 7. The adopted model parameters are $\sin i = 0.6$, $v_{bulk} = 18 \text{ km s}^{-1}$, $v_{turb} = 14 \text{ km s}^{-1}$, $v_{th H} = 14 \text{ km s}^{-1}$. Refer the text for the definitions of these parameters. This profile provides a much better fit than that shown in Fig. 6. It is noted that the expansion velocity of the H I shell is $v_{exp} = 15 \text{ km s}^{-1}$, which is significantly smaller than that considered in Fig. 6.

Table 2. He II Recombination Data by Storey & Hummer (1995)

Line Ratio	$T_e = 10^4$ K	$T_e = 2 \times 10^4$ K
$n_e = 10^4 \text{ cm}^{-3}$		
F_{1025}/F_{6560}	3.600	4.519
F_{6527}/F_{6560}	3.952×10^{-2}	4.085×10^{-2}
$n_e = 10^6 \text{ cm}^{-3}$		
F_{1025}/F_{6560}	3.804	4.676
F_{6527}/F_{6560}	4.098×10^{-2}	4.152×10^{-2}
$n_e = 10^8 \text{ cm}^{-3}$		
F_{1025}/F_{6560}	4.439	5.181
F_{6527}/F_{6560}	4.942×10^{-2}	4.614×10^{-2}